Evolving Platinum-Copper Nanostructures for Enhanced Photothermal Therapy and Controlled Copper Release in Cancer Therapy

Jose I. Garcia-Peiro, María Sancho-Albero, Silvia Miguel, Andrea Mosseri, Felipe Hornos, Rafael Contreras-Montoya, Jose L. Hueso,* and Jesus Santamaria*

Nanotechnology provides a panoply of new tools in cancer therapy, enabling advanced treatments such as chemodyamic therapy (CDT), radiation therapy (RT), photothermal therapy (PTT) or photodynamic therapy (PDT). The therapeutic effect can be increased by combining one or more of these actions and this is usually considered already from the design of the nanoparticles (NPs). Bimetallic NPs are obvious candidates in this respect, being able to trigger a multifunctional response associated to each metal and achieving a synergistic action in combined therapies. In this work, we designed platinum-copper bimetallic NPs (PtCu NPs) capable to evolve during treatment and fulfill a dual role as chemotherapeutic agents, (controlled release of ionic Cu), and as tumor ablation agents under near infrared (NIR) irradiation. Tuning the synthesis conditions demonstrated the influence of metal composition and alloying degree on the Cu release pattern when exposed to physiological media. The Cu ions released disrupt the redox balance in cells by generating reactive hydrogen species (likely hydroxyl radicals ●OH through reaction with H_2O_2 overexpressed in the tumor microenvironment) while simultaneously oxidizing glutathione (GSH). After Cu release, the remaining Pt-rich structures present enhanced photothermal (PT) response. The efficacy of the combined therapy enabled by these NPs has been evaluated in vitro and in vivo.

1. Introduction

Cancer remains as one of the leading causes of mortality worldwide, demanding continuous innovation in therapeutic strategies to improve treatment specificity, effectiveness, and safety.[1] Nanotechnology raises hopes of improving current cancer therapies by enabling precise targeting, smart delivery of therapeutic agents and multimodal therapeutic approaches.[2] Nano-platforms have been widely investigated as therapeutic agents in treatments such as chemodynamic therapy (CDT),[3] radiation therapy (RT),[4] photothermal therapy (PTT),[5] photodynamic therapy (PDT),[6] catalytic nanomedicine,[7] sonodynamic therapy (SDT)[8] or immunotherapy.[9]

Synergistic therapies, combining one or more treatment modalities to enhance therapeutic outcomes, have been in the spotlight for their ability to simultaneously target different pathways and employ complementary mechanisms of action to treat cancer.[10] When coupled with

J. I. Garcia-Peiro, M. Sancho-Albero, S. Miguel, A. Mosseri, J. L. Hueso, J. Santamaria
Instituto de Nanociencia y Materiales de Aragón (INMA)
CSIC-Universidad de Zaragoza
Campus Rio Ebro, Edificio I+D, C/ Poeta Mariano Esquillor, s/n,
Zaragoza 50018, Spain
E-mail: jlhueso@unizar.es; jesus.santamaria@unizar.es
J. I. Garcia-Peiro, M. Sancho-Albero, A. Mosseri, J. L. Hueso, J. Santamaria
Department of Chemical and Environmental Engineering
University of Zaragoza
Spain; Campus Rio Ebro, C/María de Luna, 3, Zaragoza 50018, Spain

J. I. Garcia-Peiro, M. Sancho-Albero, A. Mosseri, J. L. Hueso, J. Santamaria
Networking Research Center in Biomaterials
Bioengineering and Nanomedicine (CIBER-BBN)
Instituto de Salud Carlos III
Madrid 28029, Spain
J. I. Garcia-Peiro, M. Sancho-Albero, A. Mosseri, J. L. Hueso, J. Santamaria
Instituto de Investigación Sanitaria (IIS) de Aragón
Avenida San Juan Bosco, 13, Zaragoza 50009, Spain
J. L. Hueso
Escuela Politécnica Superior
Universidad de Zaragoza
Crta. de Cuarte s/n, Huesca 22071, Spain
F. Hornos
Instituto de Investigación
Desarrollo e Innovación en Biotecnología Sanitaria de Elche (IDiBE)
Universidad Miguel Hernández
Elche 03202, Spain
R. Contreras-Montoya
Nanoscopy-UGR Laboratory
Facultad de Farmacia
Granada 18071, Spain

nanotechnology, the potential of synergistic therapies may be further amplified.[11] In particular, nanosystems can be designed to incorporate multiple functionalities in a single vector, providing highly effective and versatile tools to advance in cancer therapy.

Among the wide variety of nanoplatforms, bimetallic nanoparticles have attracted substantial attention due to the possibility of combining the properties of different metals in a single multimodal device.[12] However, despite their potential, the smart design of these NPs remains a strong challenge.[13] One critical factor influencing the efficacy of metallic NPs is the arrangement of metals and their environment within the metallic lattice. This structural configuration can deeply affect key properties such as stability, reactivity, and functionality.[14] These characteristics have been extensively studied in fields like catalysis[15] and electrochemistry,[16] where factors such as metal composition, spatial arrangement, alloying or segregation of phases directly impact the overall performance. However, in biomedical applications, particularly for therapeutic purposes, detailed investigations into how metals are distributed in bimetallic nanoparticles and how this distribution influences their therapeutic efficiency have been scarcely studied.[13] Addressing these aspects will be key in unlocking the full potential of metallic NPs for synergistic cancer therapies.

In some cases, the design of bimetallic nanoparticles allow the release of cations from one or both metallic species, enabling a therapeutic action (e.g., through homogeneous catalysis) of the released ions.[17] Of particular interest is the release of copper ions, given their role as homogeneous catalysts. For instance, recent results from our laboratory highlighted the pattern of ionic Cu release from hybrid CuFe NPs and the subsequent disruption of tumor redox homeostasis through ROS generation and simultaneous oxidation of gluthatione.[17] Also, the ability of released Cu^{2+} ions to catalyze transamination in biological environments has been demonstrated in a recent work.[18] Understanding the mechanisms behind Cu ion release from NPs informs NP design and enables control of the release, a key factor toward future applications.[14,19]

In addition to Cu, heterogeneous Pt has been in the spotlight of anticancer therapeutic opportunities,[20] adding a new facet to the classical role-played by Pt compounds as homogeneous chemotherapeutic drugs. Particularly, the role of Pt NPs as photothermal agent has been exploited in the last few years, where mono-[14] and bimetallic[21] Pt-based NPs have been used as antitumor agents. Interestingly, the shape of Pt nanostructures influences their photothermal performance. Zhang and coworkers[14] compared Pt nanocubes, nanodendrites and nanoframes as photothermal agents. Both, experiments and simulations corroborated the superior performance of Pt nanoframes that were also applied as photothermal agent for PTT in vivo.[14]

Bimetallic PtCu NPs have previously been tested in different therapeutic modalities, including PTT,[21] X-ray enhancement[21] and sonodynamic therapy (SDT).[22] In contrast, this work focuses on the adaptive transformation of PtCu nanostructures upon exposure to physiologically relevant environments and the evolution of their physicochemical properties, enabling synergistic therapy. In our case, NP evolution drives by the enhanced release of Cu ions under conditions representative of the tumor microenvironment (TME). This evolution leads to in situ morpho-logical and compositional changes that enhance the photothermal properties of the resulting structures.[19,23] The optimized PtCu NPs start their therapeutic action by releasing Cu ions, i.e., catalytic species able to disrupt redox homeostasis in the recipient cells by simultaneously increasing the generation of reactive oxygen species (ROS) and depleting GSH levels. The Cu release process leads to a progressively Pt-enriched architecture that becomes a powerful photothermal agent because of these morphological changes. This dual-function seeks the synergistic effect of PT and chemodynamic actions derived from Pt and Cu, respectively, under conditions relevant to the tumor microenvironment (TME).[24] These therapeutic effects have been explored in vitro and in vivo (**Scheme 1**).

2. Results and Discussion

2.1. Synthesis and Morpho-Chemical Characterization of PtCu Bimetallic Nanoparticles

As stated above, our goal was to prepare hybrid PtCu NPs able to release therapeutic Cu ions and to enable photothermal action, thanks to the Pt contribution. In previous works of our laboratory[17] we demonstrated that glutathione (GSH), a molecule overexpressed in the tumor microenvironment, was able to coordinate Cu ions, triggering a preferential release of Cu from CuFe nanoparticles. Inspired by these results, we attempted to incorporate Cu into Pt-based nanostructures to enable release upon exposure to specific conditions of the tumor microenvironment. As a starting point we used the solvothermal approach reported by Kim et al[19] to produce PtCu alloys, as catalysts in the oxygen reduction reaction. While a bimetallic alloy is unlikely to release a large proportion of one or its components in a biological environment, we hypothesized that the proportion of alloyed material could be tuned by adjusting the synthesis duration. Two different reaction times were used, 3 and 5 h respectively. The results are shown in **Figure 1**. The sample reacted for 5 h, labeled as PtCu-5 h (Figure 1a) had a high Pt content, as revealed by elemental analysis (30 wt.% of Cu and 70% of Pt in the structure). TEM images revealed the formation of homogeneous polyhedral nanoparticles with average diameters close to 90 nm (Figure 1b,c; Figure S1, Supporting Information section). High-angle annular dark-field scanning transmission electron microscopy (HAADF-STEM) confirmed the generation of well-defined multi-cubic shape configurations (Figure 1d), in which Pt and Cu were homogeneously distributed, as confirmed by EDX mapping analysis (Figure 1e; Figures S2 and S3, Supporting Information). X-ray Diffraction (XRD) analysis suggests the formation of an alloyed phase due to the shift of the main diffraction peaks with respect to monometallic Pt and Cu diffraction patterns.[25] Specifically, the main peak in the XRD spectrum is centered 41.8 degrees, while the corresponding peaks for Pt (111) and Cu (111) appear at 40.2° (for Pt) and 43° (for Cu) (Figure 1f).

The pattern of Cu ion release for bimetallic PtCu-5 h NPs was obtained for different relevant environments, namely with the NPs immersed in physiological serum (FBS) and in solutions containing a 5 mM concentration of GSH (a level considered typical of different tumor cells[17]) or slightly acidic medium (a pH = 5.5, also characteristic of the tumor microenvironment, TME). The Cu release from PtCu-5 h NPs was negligible, regardless of
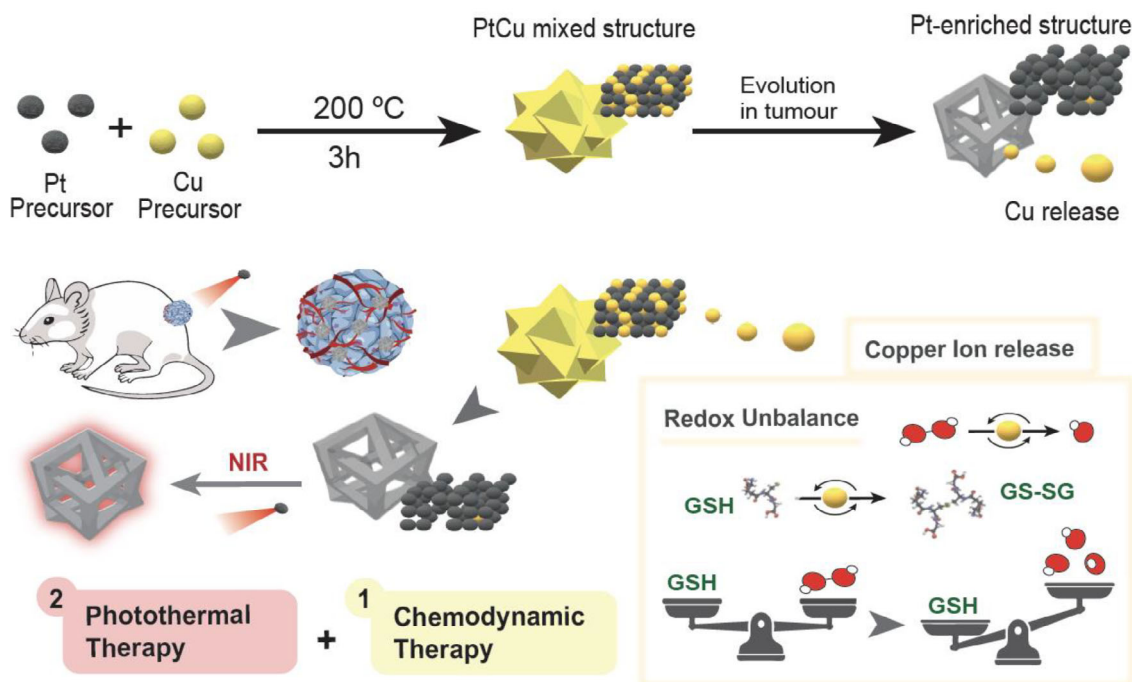
Scheme 1. Schematic illustration of the mechanisms involved in the therapeutic action of PtCu nanostructures. The synthesis uses Pt and Cu precursors to produce a mixed-metal nanostructure capable of releasing Cu ions. These are effective chemodynamic agents able to produce ROS and at the same time deplete GSH. The resulting Pt-rich nanostructure presents enhanced photodynamic properties and is an effective agent for NIR hyperthermia.

the selected environment (Figure 1m), which is consistent with a scenario where most of the Cu is alloyed with Pt.

In view of the lack of Cu release from PtCu-5 h, the synthesis reaction time was shortened to 3 h in an attempt to reduce the extent of Pt-Cu alloying. This is reasonable due to the specific reduction kinetics in the system investigated. While looking at the standard reduction potentials of Cu and Pt[26] it would be expected that Pt reduces first and then Cu, in this system the order is reversed, due to the interactions of Cu cations with biological molecules, especially those containing amino groups. In particular, glycine, which is present in the synthesis solution (see Experimental section) has been reported to modulate reduction potentials and significantly accelerates the reduction of Cu.[26,27] Thus in our system Cu^+ is reduced in the first place forming a Cu-rich core, then Pt reduction takes place, and under solvothermal conditions at 200 °C starts alloying with Cu, initially at the edges of the Cu nanoparticles, then alloying proceeds toward the bulk of the NPs until the reaction is completed. Thus, by diminishing the overall reaction time from 5 to 3 h we aimed to reduce the extent of alloying between Pt and Cu, and the nanoparticles obtained (PtCu-3 h) would be expected to contain a large pool of unreacted Cu-enriched domains with the potential to act as Cu release reservoirs.[14,27,28]

This strategy was successful, as shown in Figure 1. TEM images showed that PtCu-3 h samples consisted of homogeneous NPs with average diameters of 85 nm (Figure 1h,i; Figure S1, Supporting Information). Elemental analysis revealed that the NPs were Cu-enriched (70% wt. Cu) PtCu-3 h NPs showed multi-cubic shape configuration (Figure 1i,j), and the EDX elemental mappings clearly showed an inner Cu-enriched fraction thereby suggesting a heterogeneous bimetallic configuration

for the PtCu-3 h NPs (Figure 1k; Figures S2 and S3, Supporting Information). These results were confirmed by XRD analysis, where two separate peaks were distinguished at 41.8° and 43° respectively. The former corresponding to the PtCu alloy, as discussed and the latter attributed to non-alloyed metallic Cu excess[19,23] (Figure 1l). The Z-potential measurements revealed a surface charge of −24 mV for PtCu-3 h NPs leading to excellent colloidal stability in complex media. NTA particle size measurements in the presence of GSH and acidic pH (5%) yielded a mode hydrodynamic size of 87.2 nm, corresponding to minimal agglomeration (Figure S4, Supporting Information).

Finally, Cu release experiments (Figure 1n) showed that PtCu-3 h NPs displayed a fast discharge of Cu, in sharp contrast with the near absence of release in PtCu-5 h NPs (Figure 1m,n). It is also noteworthy that PtCu-3 h NPs revealed different release patterns depending on the environment. NPs exposed to serum approached 50% release in the first few days and longer exposure times did not induce additional release (Figure 1n). In contrast, PtCu-3 h NPs exposed to high GSH concentration or acidic pH 5.5 representative of tumor microenvironment conditions released a much higher proportion, ≈80% or higher being released in 14 h when exposed to GHS-containing or acidic environments. Additionally, Cu release experiments were performed under different concentrations of GSH (0.05, 0.5, and 5 mM) for PtCu-3 h NPs, highlighting a correlation between total copper leveraged and GSH in the samples (Figure S5, Supporting Information).

In slightly acidic environments (pH 5.5), copper ions are released faster from PtCu nanostructures compared to neutral pH, due to the oxidation of metallic copper (Cu^0) to Cu^{2+}. This process is well documented in the literature, with dissolution rates increasing one order of magnitude per every 0.5 units of pH
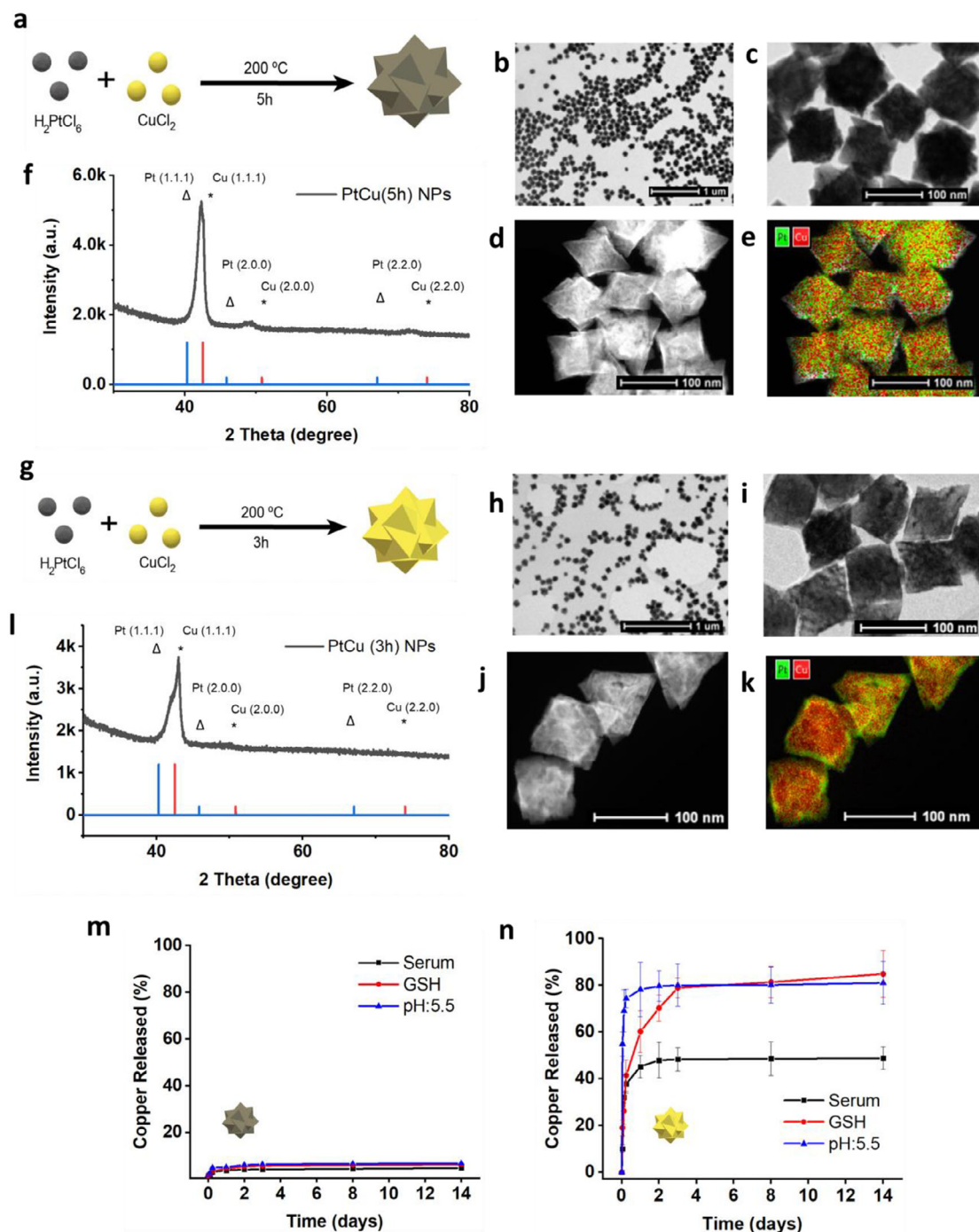
Figure 1. a) Schematic illustration of PtCu NPs synthesis using solvothermal method for 5 h to obtain alloyed PtCu NPs, b) Representative TEM images of PtCu (5 h) NPs, c) TEM, d) HAADF-STEM, and e) HAADF-STEM mediated EDX mapping images of alloyed PtCu NPs, f) X-ray diffraction patterns of PtCu (5 h) NPs and their comparison with metallic Pt and Cu diffraction patterns. We can observe peaks correlated with Pt and Cu alloys with a shift in the well-defined crystal lattice planes, indicating the formation of Pt/Cu alloys, g) Schematic illustration of PtCu NPs synthesis using solvothermal method for 3 h to obtain bimetallic PtCu NPs, h) Representative TEM images of PtCu (3 h) NPs, i) TEM, j) HAADF-STEM and k) HAADF-STEM mediated EDX mapping images of alloyed PtCu NPs, l) X-ray diffraction patterns of PtCu (5 h) NPs and their comparison with metallic Pt and Cu diffraction patterns. We can observe an extra peak correlated with metallic Cu indicating the partial formation of Pt/Cu alloys in the structure, m) Copper ions release properties of PtCu (5 h) NPs when exposed to serum, GSH (5 mM) and acidic pH (5.5) for 14 days, n) copper ions release properties of PtCu (3 h) NPs when exposed to serum, GSH (5 mM) and acidic pH (5.5) for 14 days.

e02999 (4 of 15)

**ADVANCED
SCIENCE NEWS**

www.advancedsciencenews.com

**ADVANCED
FUNCTIONAL
MATERIALS**

www.afm-journal.de

decrease[11c]. Additionally, the thiol groups in GSH coordinate with Cu, facilitating its complexation and promoting a strong acceleration of the release of Cu^{2+} ions as coordination complexes into the solution.[17,29] This behavior cannot be observed in fully alloyed PtCu NPs because in these structures, Cu and Pt are uniformly distributed across the NP, forming stable, intermetallic bonds.[23,30] Thus alloying stabilizes copper and prevents it from being oxidized or complexed and released under physiological conditions. In contrast, in Cu-enriched PtCu structures, non-alloyed copper is present, as shown in Figure 1, with a behavior similar to that of metallic copper.

In view of this, PtCu-3 h NPs (hereafter termed simply PtCu NPs) were chosen for all subsequent studies.

2.2. Cu Release Leads to Pt-Enriched Hollow Nanoframes with Enhanced NIR-Photothermal Response

PtCu NPs (i.e., PtCu-3 h NPs) were subjected to Cu release and then characterized by HAADF-STEM and EDX mapping analysis (**Figure 2a–c**). The structures evolved into Pt-enriched partly-hollow nanoframes (PtCu NFs) (Figure 2a–c; Figure S6, Supporting Information). In contrast, HAADF-STEM analysis of PtCu-5 h NPs indicated that the morphology and composition remained unaltered after prolonged contact with GSH (5 mM) (see Figures S6 and S7, Supporting Information). MP-AES measurements corroborated the extent of Cu release since the Cu content diminished from 70% to 18 wt.% after exposure to GSH 5 mM for 24 h (Figure 2d; Figure S8, Supporting Information). XRD analysis of the PtCu NFs also confirmed a significant decrease of the diffraction peak attributed to metallic Cu at 43° (Figure 2e; Figure S9, Supporting Information).

The PtCu NPs and the Pt NFs displayed a broad absorption band throughout the visible-NIR range (Figure S10, Supporting Information). It is noteworthy that the hollow Pt frames yielded a specific absorption increase in the NIR window underlying the influence of the Pt morphology.[20] This is in agreement with the findings of Zhang and co-workers,[14] who demonstrated the strong effect of morphology on NIR light absorption, with best results obtained for the frame-like shapes. The procedure described in this work allows the in situ carving of partly hollow Pt-enriched NFs as the particle evolves thanks to the progressive Cu release under physiological conditions.

We carried out a systematic study to explore the PT response of the PtCu NPs and the Pt NFs. We compared the PT properties of PtCu-3 h NPs before and after Cu release under NIR light irradiation ($\lambda = 808$ nm). Remarkably, while the PtCu NPs already had considerable PT activity, as it can be seen in Figure 2f, the in situ generated Pt NFs displayed a significantly better PT performance. In addition, a clear dose-dependent PT response was found for the Pt NFs (Figure 2g). It is worth noting that, in contrast to their Au analogs, Pt NPs seem able to induce photo-induced thermal heating regardless, which is also in agreement with the results of Zhang et al.[23] In our case, we leveraged conditions prevailing in the tumor environment to in situ generate Cu-deficient Pt-rich scaffolds with enhanced PT properties.

As expected the heat generation of PtCu NFs displays a correlation with the irradiation power, rising progressively as this
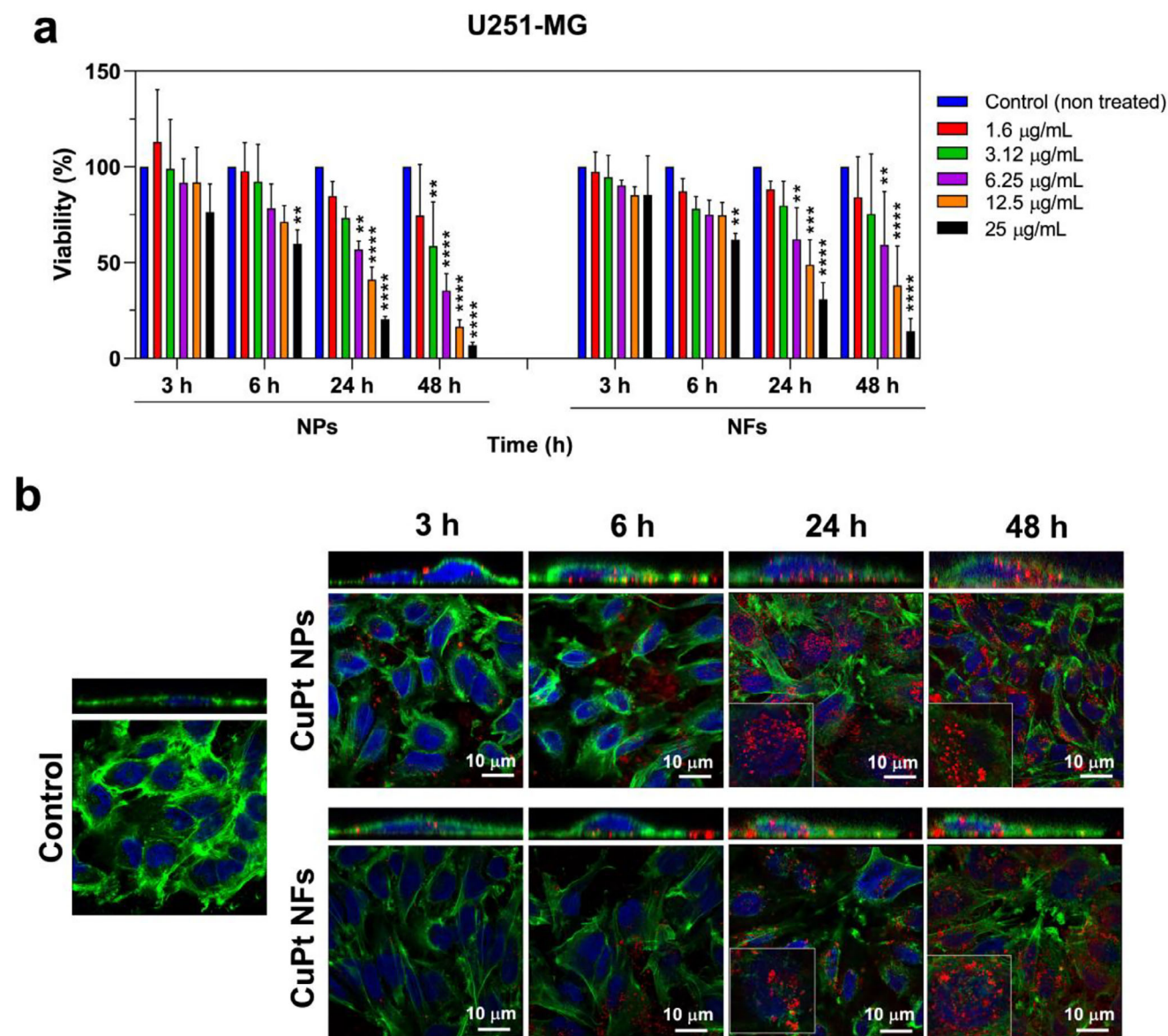
was increased from 0.5 to 2 W (Figure S11, Supporting Information). The PT properties of PtCu NFs have also been compared with other NIR-sensitive nanostructures (Figure S12, Supporting Information), displaying a significantly higher heating capacity thanks to the increased absorption at the wavelength used (Figure S10, Supporting Information). This enhanced heating is in agreement with previous results in the literature by Wang et al.[14] The internal structure of the PtCu NFs results in a high number of internal interfaces, which enhances the collective electrons oscillation at the metal surface.[14] These interfaces likely contribute to a more intense light absorption if comparing to simpler or differently shaped structures as small Pt NPs or Pt dendrites.

In addition, we evaluated the role of the Cu released as homogeneous catalysts in the Fenton reaction and the GSH oxidation.[17] GSH oxidation was monitored with the aid of DTNB, also known as Ellman's reagent.[22] The progressive disappearance of GSH was indirectly monitored by UV–vis spectroscopy following the reduction of the absorption band centered at 412 nm and the relative increase of the absorption band centered at 320 nm, corresponding to the oxidized product, GSSG.[17] (Figure 2h). The former is associated to the quantifiable fraction of TNB^{2-} that forms upon the S-S bond break of DTNB induced by GSH. As GSH converts to GSSG thanks to the catalytic action of Cu cations[17] the TNB^{2-} intermediate decreases, providing a direct measurement of catalytic activity (Figure 2h). The variation of TNB^{2-} concentration indicated a total GSH consumption (starting from 5 mM) after 24 h in the presence of O_2. On the other hand, hydroxyl radical formation via Fenton reaction of Cu[31] was also evaluated under neutral and acidic conditions (pH 5.5 and 7.4). TMB was selected as colorimetric probe to identify the potential generation of reactive oxygen species (ROS) in the presence of H_2O_2.[31] As can be observed in Figure 2i, the activity of the Cu released from PtCu NPs for ROS production was significantly higher under acidic conditions.

Lastly, we also evaluated the catalase-like activity of Pt hollow NFs in the generation of O_2 from H_2O_2. The reaction was performed at room temperature and also at a higher bulk (i.e., solution) temperature of 42 °C, achieved either by immersion in a water bath at this temperature, or by subjecting the NF suspension to illumination under irradiation at 0.44 Wcm^{-2} with 808 nm NIR light. In Figure 2j, we observed how PtCu NFs efficiently perform catalase-like reaction generation O_2 even at room temperature. As expected, when the temperature increased by conventional heating to 42 °C, the catalytic rate increased accordingly. However, when the same bulk temperature of 42 °C was achieved by irradiating PtCu NFs with NIR light, a remarkably higher reaction rate was observed. This increase can be attributed to a local overheating of the catalytic sites in the PtCu NFs with respect to the bulk temperature. In summary, the results of this section show the catalytic activity (for GSH oxidation and in Fenton-like reactions for ROS generation) of the Cu cations released by PtCu NPs under the low pH conditions characteristic of the TME or of specific acidic domains such as lysosomes.[24] The catalase-like activity of the PtCu NFs generated in situ after Cu release strongly increased when the PtCu NFs were subjected to NIR irradiation.
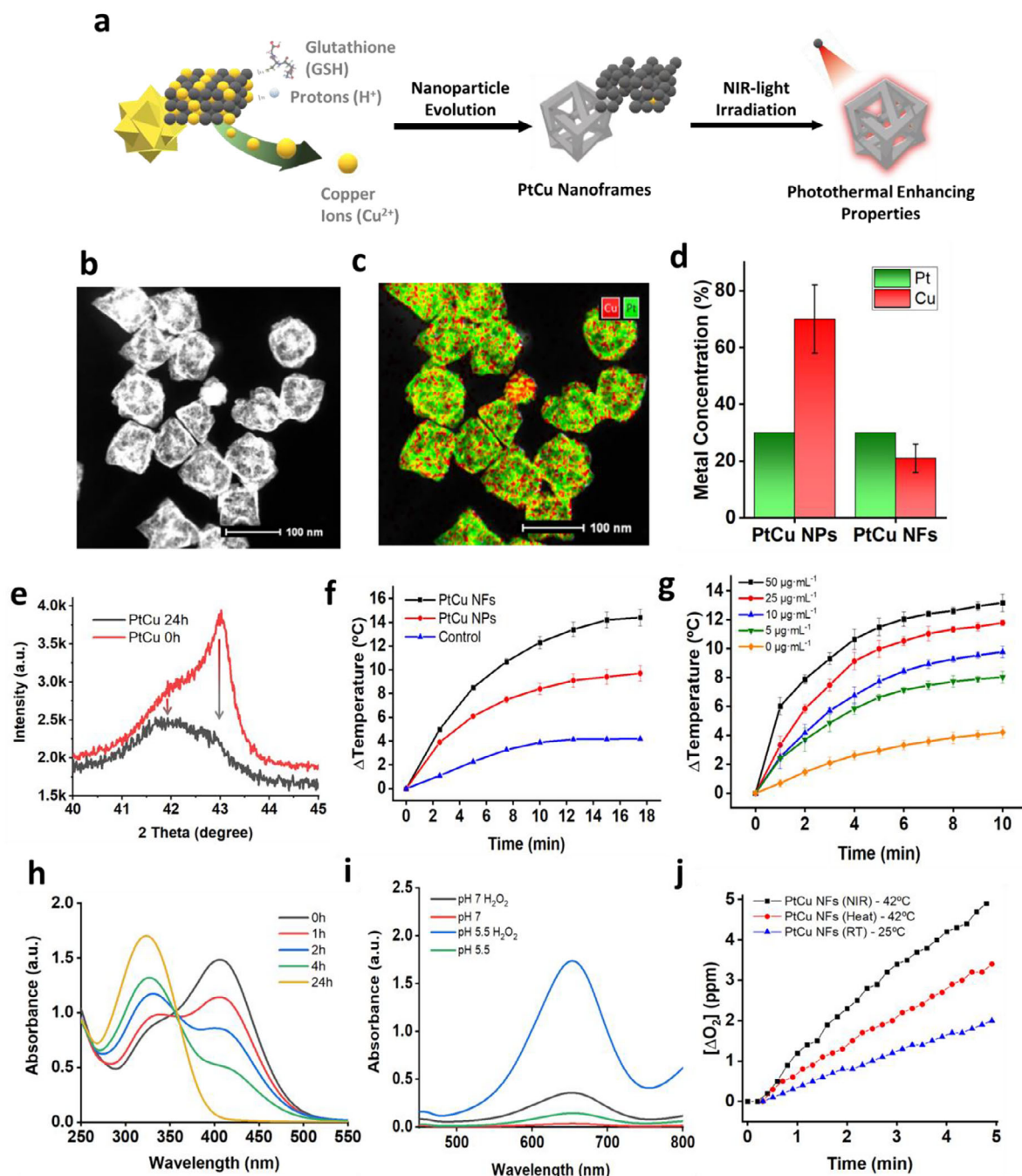
Figure 2. a) Schematic illustration of the Cu-releasing process of PtCu-3 h NPs when exposed to GHS-containing or mildly acidic environments. PtCu-3 h NPs release copper and evolve into PtCu nanoframes with enhanced photothermal properties. b) HAADF-STEM images of PtCu nanoframes after treating PtCu-3 h NPs with GSH (5 mм) for 24 h, c) HAADF-STEM mediated EDX mapping images of PtCu nanoframes after treating PtCu-3 h NPs with GSH (5 mм) for 24 h, d) Elemental analysis of PtCu-3 h NPs before and after treatment with GSH, e) XRD evolution of PtCu-3 h NPs after 24 h exposure to 5 mм GSH. A strong decrease in intensity of Cu (111) peak can be observed as a consequence of Cu release, f) Temperature rise caused by NIR irradiation in a suspension of PtCu NPs before and after Cu release (i.e., PtCu NFs) (808 nm, 0.44 Wcm^{-2}, 2 mL total volume, and 0.05 mg mL^{-1}). g) Dose-dependent photothermal behavior of PtCu NFs when exposed to NIR light (808 nm, 1 W cm^{-2} and 2 mL total volume) at different concentrations, h) Evaluation of GSH depleting properties of Cu released from PtCu NPs with DTNB as the trapping agent of sulfhydryl group in GSH (5 mм), i) Fenton-like properties of released ionic Cu from PtCu NPs revealed by UV–vis spectroscopy of acetate (pH 5.5)/PBS (pH 7.4) buffer solution in presence of TMB, j) Catalase-like activity of PtCu NFs for H$_2$O$_2$ (1 mM) decomposition to release O$_2$.

ADVANCED
SCIENCE NEWS
www.advancedsciencenews.com

ADVANCED
FUNCTIONAL
MATERIALS
www.afm-journal.de

Figure 3. a) Cytotoxicity of PtCu NPs and PtCu NFs in U251-MG cells. Results are expressed as mean ± SD ($n = 3$). Statistically significant differences were expressed as follows: $^*p < 0.05$; $^{**}p < 0.01$; $^{***}p < 0.001$ y $^{****}p < 0.0001$. b) Internalization of PtCu NPs and PtCu NFs in U251-MG cells. Cells were labeled with phalloidin-Alexa488 to stain the cytoskeletal actin fibers (green) and with DAPI for the nuclei (blue), respectively. Confocal Z-stacks of cells incubated with the nanoparticles (6.25 µg mL^{-1}) during 3, 6, 24, and 48 h. The insets and the orthogonal projections show that red-visualized particles are surrounded by green actin fibers inside the cell cytoplasm.

2.3. Cytotoxicity, Internalization and In Vitro Cell Death Assays of PtCu NPs for Different Cancer Cell Lines

PtCu NPs and Pt-enriched NFs were tested for cytotoxicity on U251-MG, HeLa and B16-F10 cells. NPs and NFs were incubated during 3, 6, 24, and 48 h and using different concentrations of NPs (from 1.6 to 25 µg mL^{-1}).). **Figures** 3a and S13a (Supporting Information) show that in the case of HeLa and B16-F10 cells, no significant decrease in their viability was detected at the initial incubation time intervals (3 h and 6 h). In contrast, in the case of U251-MG cells, both types of Pt structures induced a significant reduction of cell viability for the highest NPs doses (25 µg mL^{-1})

after 6 h of incubation in a concentration- and time-dependent way after 24 and 48 h of treatment, respectively (Figure 3a; Figure S13a, Supporting Information).

The internalization of PtCu NPs and PtCu NFs in U251-MG, HeLa, and B16-F10 cells was further evaluated by confocal microscopy. Both nanostructures were incubated with the cells at 6.25 µg mL^{-1} for 3, 6, 24, and 48 h. PtCu NPs and PtCu NFs were directly observed by reflection of the incident light (red). NPs were clearly internalized forming aggregates inside the cytoplasm, and probably inside vesicles following the endosomal route as reported in the literature.[32] Whereas after 3 and 6 h of incubation, particles were attached to cell membrane starting
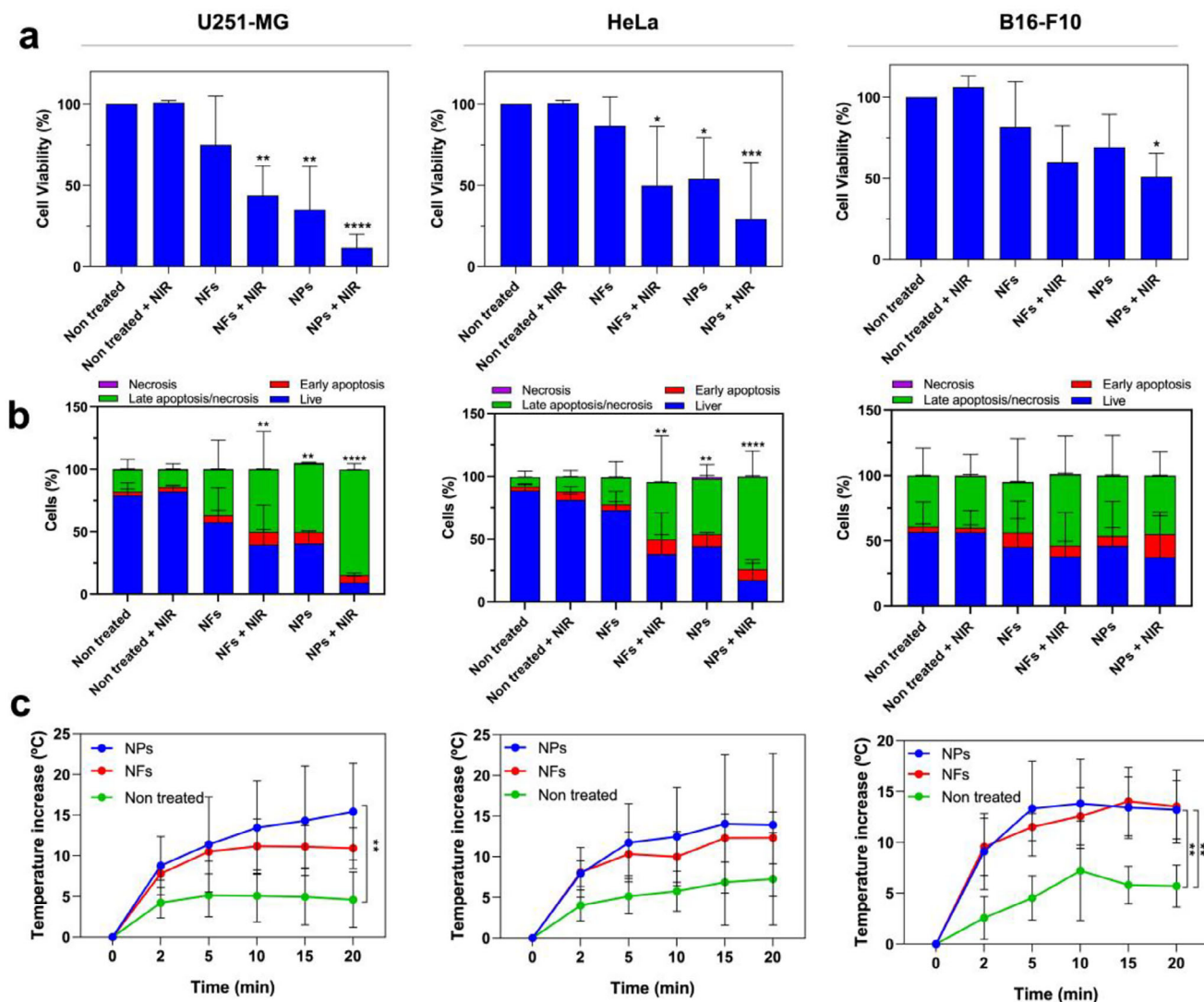
Figure 4. a) Cell death effect measured by Cell Blue Assay and mediated by the PtCu NPs and the PtCu NFs in the presence or absence of NIR laser irradiation. b) Cell Apoptosis evaluation by flow cytometry after treatment with PtCu NPs and PtCu NFs and with or without NIR laser irradiation. c) Cell culture temperature increase of non-treated, PtCu NFs-treated, and PtCu NPs-treated cells. Results are expressed as mean $\pm$ SD ($n = 3$). Statistically significant differences were expressed as follows: $^*p < 0.05$; $^{**}p < 0.01$; $^{***}p < 0.001$ y $^{****}p < 0.0001$.

their internalization, the fluorescence of the particles within cells significantly increased after 24 and 48 h of incubation in all the tested cell lines (see orthogonal projections in Figure 3b and Figure S13b, Supporting Information).

In order to evaluate the potential synergistic effect of Cu and Pt, we tested the in vitro therapeutic efficacy of both PtCu-3 h NPs and the Pt-enriched NFs. U251-MG, HeLa, and B16-F10 cells were incubated with the NPs during 24 h, to ensure the release of Cu. Then, after washing, cell cultures were irradiated with an 808 nm NIR laser for 20 min. Cell viability was estimated by Cell Blue Assay (CBA) and apoptosis/necrosis death mechanisms were determined by flow cytometry. NIR laser irradiation experiments in the absence of PtCu NPs or NFs did not cause any significant cell death (**Figure 4a**). Also, the PtCu NFs did not affect the cell viability in the absence of NIR light (Figure 4a) and exhibited similar behavior as the control, non-treated cells.

In contrast, when the NIR laser was applied to the cell cultures treated with the PtCu NFs a strong reduction of cell viability was observed in the case of U251-MG and HeLa cells (Figure 4a). Remarkably, PtCu NPs were able to induce significant cell death in the absence of NIR irradiation, although only for U251-MG and HeLa cells, reducing cell viability to 35% and 54% in the case of U251-MG and HeLa cells, respectively. In addition, after irradiation cell viability of U251-MG and HeLa cells, decreased to 29.3% and 11.47%, respectively. These trends were qualitatively confirmed by observations in an optical microscope (Figure 4a; Figure S14, Supporting Information). These results confirmed the synergistic effect of the combined therapies: CDT mediated by Cu ions released by PtCu NPs followed by PT treatment on the Pt-enriched NFs. On the other hand, the NFs effect was largely confined to cell death by local heating since there is little or no Cu to be released (Figure 4a).

**ADVANCED
SCIENCE NEWS**

www.advancedsciencenews.com

**ADVANCED
FUNCTIONAL
MATERIALS**

www.afm-journal.de

The evaluation of cell apoptosis and necrosis by flow cytometry on cells treated with PtCu NPs or PtCu NFs and/or NIR laser irradiation is presented in Figure 4b. In general, these results confirmed the trends observed from the cell viability data, just discussed. For the case of B16-F10 cells, no significant effect on cell apoptosis and necrosis was observed under any of the conditions investigated. However, while no statistical significance could be obtained, B16-F10 cells treated with PtCu NPs and NIR laser irradiation displayed a slight increase in early apoptosis compared to the control samples (Figure 4b; Table S1, Supporting Information). In contrast, the U251-MG and HeLa cells containing the Pt-enriched NFs, showed a significant increase of the late apoptosis/necrosis after NIR irradiation (Figure 4b; Table S1, Supporting Information, temperature increases in Figure 4c). In addition, in the case of U251-MG and HeLa cells treated with PtCu NPs, a significant increase on late apoptosis/necrosis was clearly observed even in the absence of NIR light. This can be attributed to multiple catalytic effects of Cu cations released inside the cells as previously addressed (vide supra), including ROS generation, GSH depletion, ferroptosis and cuproptosis, with a direct effect on tumor cells.[17,32,33] Finally, when irradiating U251-MG and HeLa cell cultures with the NIR laser the synergistic effect of the proposed therapeutic approach was clearly detected. A significant increase on late apoptosis/necrosis was evidenced (Figure 4b; Table S1, Supporting Information).

2.4. Intracellular GSH and ROS Quantification

To assess the effect of released Cu in intracellular GSH depletion, GSH levels were quantified inside U251-MG, HeLa and B16-F10 tumoral cell lines after their treatment with PtCu NPs. In all cell lines, a very significant decrease on GSH intracellular levels when treated with CuPt NPs was observed compared to untreated control cells (Figure S15a, Supporting Information). In addition, the production of intracellular ROS following NP uptake was also assessed using a commercial ROS probe, as described in the experimental section. Figures S15b,c (Supporting Information) demonstrate that the release of Cu cations also induced a very significant increase of intracellular ROS production. This increase could not be balanced by the antioxidant action of GSH that is simultaneously being depleted, as shown by the results from Figure S15a (Supporting Information). The increase in ROS upon exposure to NPs was significant for all cell lines, but especially noteworthy in U251-MG, that exhibited the higher levels of intracellular ROS production and the strongest cytotoxic effect of the PtCu NPs. The weaker ROS generation in B16F10 cells could be in part explained by the lower internalization of the nanoparticles in this cell line, as can be seen in Figure S13 (Supporting Information). In contrast, the degree of internalization in HeLa and U251-MG cell lines is similar (Figure S13, Supporting Information), but the cytotoxicity is significantly higher toward U251-MG cells, which is in agreement with the higher intensity of ROS generation observed in Figure S15 (Supporting Information).

2.5. In Vivo Combined CDT-PTT Treatment with PtCu NPs

Before the therapy experiments, PtCu NPs were administered intratumorally in a xenograft murine model, as described in the ex-

perimental section. The objective was to evaluate the amount of metals remaining in the tumor after injection and their possible migration to other organs. To this end, the amount of Cu and Pt in the different organs was measured by ICP-MS after organ digestion. The results shown in **Figure 5a**, revealed that the majority of the Cu and the Pt were localized in the tumors after 24, 48 h, and 1 week of their intratumoral administration. In contrast, a very low percentage of the administered NPs localized in the liver, spleen, pancreas, lungs, and kidneys. Figure 5b shows confocal microscopy images after immunofluorescence labeling of tumor tissues (nuclei of cells in blue labelled with DAPI and PtCu NPs observed by reflection of the incident light in red), again confirming that PtCu NPs mostly retained in the tumoral tissue even after 1 week of their administration. Finally, histopathological analysis of HE stained sections of tumors and other tissues of animals treated with the PtCu NPs (Figure S16, Supporting Information) did not reveal significant cellular morphological alterations that could be attributed to the accumulation of the NPs in any of the tissues studied, when compared to control mice. In the tumors (Figure 5c), the presence of the particles was clearly observed as black aggregates within the tumoral mass.

For the therapy experiments, tumor cells were inoculated in a xenograft model and tumor growth was followed until the ethically allowed size was reached. As **Figure 6a** indicates, tumor size for animals of the two control groups (non-treated-mice and NIR- irradiated mice) increased rapidly over time. In the case of the PtCu NPs-treated mice, tumor growth was arrested for ≈48 h after each injection of the NPs, indicating the therapeutic effect of Cu ions release from the NPs. Eventually, growth started again, once the effect subsided, in spite of the fact that over half of the injected Cu likely remained in the tumor, as previously shown in Figure 5a. In contrast, tumors in the group treated with PtCu NPs and irradiated with NIR laser strongly reduced their size (Figure 6a,b). These results demonstrated the synergistic effect of Cu ions from the NPs framework and the PT effect of the Pt-rich NFs induced upon NIR irradiation. Tumor weight at the end-point of the experiment was measured and compared among the different groups (Figure 6a,b). Again, mice treated with PtCu NPs and irradiated with the NIR laser presented the smallest tumors. Figure 6b includes external and *ex vivo* images of the tumors borne by mice from the different groups. In the case of the PtCu NPs treated mice, it was possible to observe that tumors exhibited a black color, attributed to the presence of the NPs. In addition, inflammation and white areas could be observed in the subcutaneous tumor in the case of the NPs+NIR group, immediately after the application of the NIR laser, due to temperatures reached under NIR light. These temperatures could be externally measured using infrared thermal images (Figure S17, Supporting Information) showing that, under irradiation, the external temperature of skin over the tumor rapidly increased in the presence of PtCu NPs from 34 to 58 °C in 30 s, while in animals subjected to laser irradiation in absence of PtCu NPs the temperature increased from 33 to 38 °C under the same conditions. One week after the NPs+NIR treatment, the wound was well recovered and healed by formation of new skin tissue while tumor size was greatly reduced (and in some cases disappeared).

To confirm the efficacy of the antitumoral treatment mediated by PTT, a histopathological analysis comparing control
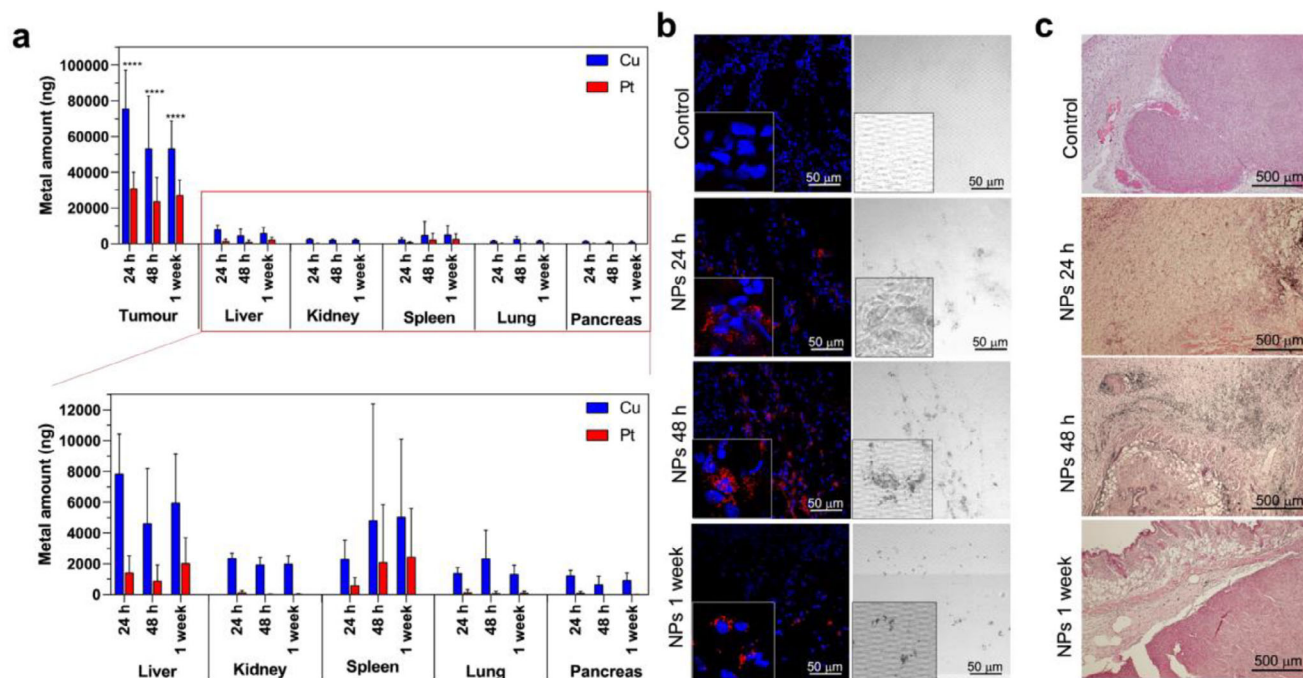
Figure 5. Biodistribution of PtCu NPs after intratumoral injection (5 mg kg^{-1} of NPs) in a xenograft murine model. a) ICP-MS analysis of Cu and Pt in organs extracted from mice after 24 , 48 h, and 1 week of NPs administration. Results are expressed as mean ± SD. Statistically significant differences were expressed as follows: $^*p < 0.05$; $^{**}p < 0.01$; $^{***}p < 0.001$ y $^{****}p < 0.0001$. b) Confocal microscopy images after immunofluorescence labeling of tumor tissues of untreated mice, and mice treated with PtCu NPs and sacrificed after 24 , 48 h, and 1 week of their administration. The nuclei of the cancerous cells were marked with DAPI and appear in blue, while the NPs were observed by reflection of the incident light as red aggregates in the cytoplasm of these cells. c) Hematoxylin and eosin tissue sections from tumors of control (untreated) and PtCu NPs-treated mice at 24 , 48 h, and 1 week after intratumoral NPs administration.
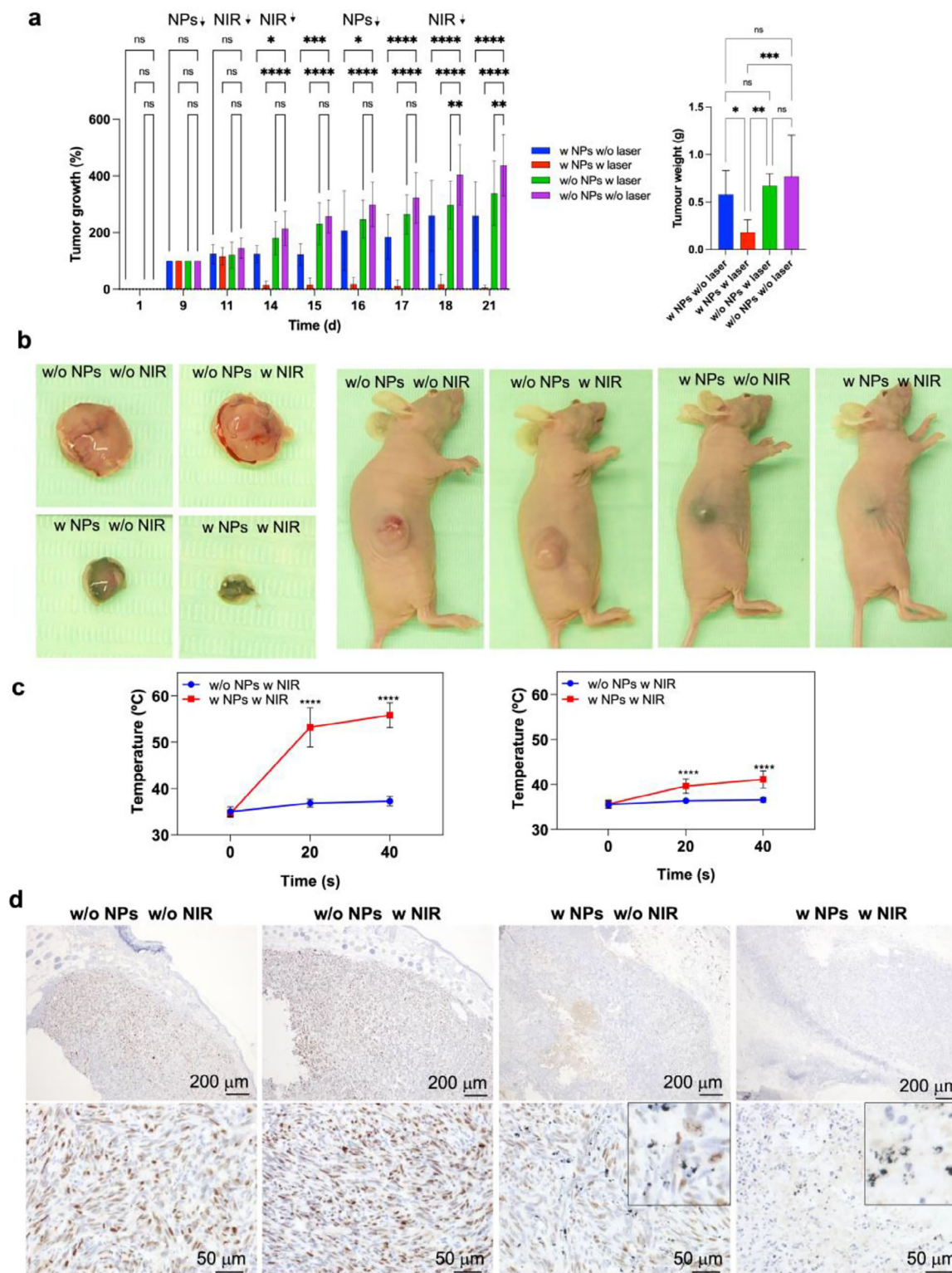
groups with the treated group was carried out by Ki-67 (a nuclear biomarker for cell proliferation that correlates with an increased growth rate and aggressiveness of tumoral cells[34]). Figure 6d indicates that, in the case of the control groups (mice non-treated with laser and non-treated with PtCu NPs and mice irradiated but in the absence of PtCu-3 h NPs) almost all tumoral cells were strongly positive, corresponding to active proliferation status. However, the signal was very strongly reduced for PtCu NPs treated tumors, with only sporadic groups of positive cells remaining. Finally, when mice were treated with PtCu NPs and then irradiated with NIR light, the Ki-67 positive cells decreased even further, demonstrating the synergistic efficacy of the proposed PTT strategy.

Finally, caspase 3 and CD40 immunohistochemistry in the tumors of mice from the different groups were carried out for the evaluation of apoptosis and necrosis, respectively (Figure S18, Supporting Information). The results show that NPs produce a clear effect in tumor sites of mice treated with NPs and then irradiated with the NIR laser, leading to the death of tumor cells mainly through induction of necrosis. In fact, this was an expected result, since necrosis has been described as the primary mechanism for PTT-induced cell death in other tumor cells.[35] Interestingly in the enlarged areas of Figure S18 (Supporting Information), NP agglomerates could be clearly observed in the cytoplasm of the necrotic cells. In contrast, in control groups almost all the cells survived the treatment, exhibiting few cells positive for apoptosis and necrosis labelling. Also, immunohistochemi-

cal staining of CCR2 and CD45R was conducted to evaluate if the presence of the intratumorally administered NPs and/or NIR laser irradiation alone was leading to significant inflammation and/or immune activation in the different tissues (Figure S19, Supporting Information). The results, as shown in Figure S19 (Supporting Information) suggested no significant alterations on the expression of CCR2 and CD45R in any of the tested tissues.

3. Conclusion

By changing the synthesis conditions, bimetallic PtCu NPs can be prepared with different patterns of Cu release under physiologically relevant conditions. As shown previously in the literature, this release of Cu cations activates chemotherapeutic pathways, triggering ROS generating reactions such as hydroxyl radical formation through reaction with H_2O_2 overexpressed in the tumor or superoxide radical by reaction with dissolved oxygen. At the same time, it promotes glutathione (GSH) oxidation, further contributing to the redox unbalance within the cell. In addition, the Cu release transforms the properties of the PtCu NPs, evolving in situ toward a Pt-rich structure with a frame-like configuration that is able to absorb NIR light with a higher efficiency than the starting material. The resulting Pt-rich nanoframes exhibit significantly improved NIR photothermal responsiveness compared to other Pt-based NPs with different morphologies. This approach parallels the work of Wang et al.[14c] who achieved similar frame-like architectures via direct nanoframe synthesis.

ADVANCED
SCIENCE NEWS

www.advancedsciencenews.com

ADVANCED
FUNCTIONAL
MATERIALS

www.afm-journal.de

Figure 6. CDT-PTT synergistic treatment: in vivo studies of xenograft tumor evolution mediated by PtCu NPs. The days for administration of PtCu NPs and NIR irradiation are indicated by arrows. $n = 8$ mice/group a) tumor growth evolution (left) and average tumor weight (right) of tumors treated with (w) and without (w/o) NIR irradiation and PtCu NPs. The tumors were collected and weighted at the end of the 21-day treatment. b) Images of tumors ex vivo and of the corresponding animals after different treatments. c) External skin temperature measured in tumors during NIR (808 nm, 1.5 W) light irradiation with and without treatment with PtCu NPs. d) Ki-67 staining in tumors from mice from the different groups, results are expressed as mean $\pm$ SD. Statistically significant differences were expressed as follows: $^{*}p < 0.05$; $^{**}p < 0.01$; $^{***}p < 0.001$ y $^{****}p < 0.0001$.

**ADVANCED
SCIENCE NEWS**

www.advancedsciencenews.com

**ADVANCED
FUNCTIONAL
MATERIALS**

www.afm-journal.de

However, our strategy enables the formation of these structures under biologically relevant conditions, in a dynamic process that involves the release of therapeutic cations to develop a highly efficient photothermal structure.

The possibility of this dual action was already determined by the conditions of NP synthesis, where the degree of alloying between Cu and Pt was regulated. Completely alloyed PtCu NPs were not able of ion release, however, partially alloyed PtCu NPs successfully leached most (ca. 80%) of their Cu content under physiological conditions. In vitro and in vivo experiments corroborated the successful translation of the combined therapy enabled by PtCu bimetallic NPs, leading to near complete tumor eradication. However, the results presented in this work are at still at the proof-of-concept stage. Moving these nanostructures toward clinical translation would entail a substantial redesign of the vector, likely by enclosing Pt and Cu domains in a biodegradable structure. The redesign of the nanoparticle would also necessarily include tumor-targeting elements, something that is not considered in this work because only intratumoral injection was used to test in vivo the efficacy of the particles themselves, without interference from the lack of delivery efficiency.

4. Experimental Section

Chemicals: Platinum (iv) chloride H_2PtCl_6 acid solution (8% wt), copper (II) chloride dihydrate ($CuCl_2 \cdot 2H_2O$, $\geq$ 99.0%), glutathione ($\geq$98, HPLC), glycine (98%), 3,3',5,5'-tetramethylbenzidine (TMB, $\geq$95%), 5,5'-Dithiobis(2-nitrobenzoic acid) (DNTB), hydrogen peroxide (H_2O_2, 33% v/v), sodium hydroxides (NaOH), polyvinylpyrrolidone (PVP, M.W. = 10000 Da), dimethyl sulfoxide (DMSO) and PBS pellets were purchased from Sigma–Aldrich (Darmstadt, Germany) and used without further purification. Water was obtained from a Milli-Q Advantage A10 System with resistivity of 18.2 mΩ (Merk Millipore, Germany).

Synthesis of PtCu Nanostructures: PtCu nanostructures were fabricated by a solvothermal method using stainless steel autoclaves. In a typical synthesis, 266 μL of H_2PtCl_6 solution (8 wt% in H_2O) was added to 4.33 mL of water solution containing 440 mg of polyvinyl polyvinylpyrrolidone (PVP, 10.000 M.W.), 180 mg of glycine and 8.7 mg of $CuCl_2$. The mixture was sonicated for 5 min and transferred to a 50 mL Teflon-lined autoclave. Then, the autoclave was immediately heated up to 200 °C for either 3 or 5 h. After reaction, the autoclave was cooled down to room temperature overnight. The resulting suspension centrifuged and washed with Milli Q water (8000 rpm, 10 min, 2 times). Pt/Cu ratio was tuned by increasing the reaction time in the synthesis. The synthesis of these materials was performed by the Synthesis of Nanoparticles Unit (UNIT 9) of the ICTS "NANBIOSIS" at the Institute of Nanoscience and Materials of Aragon (INMA)-Universidad de Zaragoza.

Synthesis of Dendritic Pt NPs: In an 8 mL glass vial, 40 mg of Pluronic F-127 and 412 μL of H_2PtCl_6 were dispersed in 4 mL of deionized water. Separately, 70 mg of A.A. was dissolved in 2 mL of water and then added to the previously prepared mixture containing the metal precursor and surfactant. The final suspension was incubated at 37 °C overnight. Unreacted precursors and byproducts were removed through two centrifugation steps (8,000 rpm, 10 min, room temperature) using 2 mL of water per cycle.

Synthesis of Small Pt NPs: In a 250 mL three-neck round-bottom flask, 100 mg of PVP was dissolved in 50 mL of deionized water. Subsequently, 255 μL of H_2PtCl_6 and 22.5 mL of ethanol were added to the solution, which was then heated to 85 °C overnight. To remove unreacted precursors, the product was subjected to two centrifugation cycles (Amicon) at 5500 rpm for 50 min at room temperature, using 20 mL of water per cycle.

Synthesis of Au NRs: The seed solution was prepared by adding 0.6 mL of freshly made, ice-cold $NaBH_4$ (0.01 M) to a mixture of $HAuCl_4 \cdot 3H_2O$

(29 μL, 0.086 M) and CTABr (10 mL, 0.1 M), followed by vigorous stirring for 2 min and aging at room temperature for 30 min. For the growth solution, CTAB (3.6 g) and 5-bromosalicylic acid (0.44 g) were dissolved in 100 mL of warm water (55 °C). After adding 1.92 mL of $AgNO_3$ (0.01 M) and letting it rest at 25 °C for 15 min, 100 mL of $HAuCl_4 \cdot 3H_2O$ (1 mM) was introduced. Following gentle mixing for 15 min, 0.512 mL of ascorbic acid (0.1 M) was stirred in until the solution became colorless. Finally, 0.32 mL of seed solution was added, stirred for 30 s, and left undistributed overnight at 27 °C.

Cu release from PtCu Nanostructures: PtCu nanostructures were adjusted to 0.1 mg mL^{-1} concentrations in 20 mL vials containing different testing solutions. The solutions were stirred at 400 rpm for different time intervals. 200 μL aliquots were collected and centrifuged at 10 000 rpm for 2 min. The resulting pellets and supernatants were transferred to separate Eppendorf tubes. Immediately, samples were treated with aqua regia, diluted with Milli Q water and analyzed to determine the percentage of metals released. Pt and Cu concentrations were determined with the aid of an Agilent 4100 MP-AES instrument.

Catalytic Conversion of Glutathione (GSH):   The potential oxidation of GSH catalyzed by the Cu cations released from PtCu NPs was evaluated in a 3 mL multi-well plate, using 2.5 mL of PBS buffer with a concentration of 0.05 mg mL^{-1} of the NPs. Additionally, 126 μL of a stock solution containing 6 mg mL^{-1} of GSH was added to the wells. The quantification of GSH was monitored using Ellman's reagent (DTNB).[17] The evolution of absorbance peaks both at 320 nm and 412 nm was monitored by UV–vis spectroscopy. 100 μL aliquots were taken at regular intervals and collected over 900 μL of PBS in Eppendorf tubes. 15 μL of a 2.2 mg mL^{-1} solution of Ellman's reagent (DTNB) in H_2O:ACN (1:1) were used.[17]

Generation of Reactive Oxygen Species (ROS):   The Fenton-like reaction of released Cu ions from bimetallic PtCu NPs was tested using 3,3',5,5'-Tetramethylbenzidine (TMB) as a probe molecule.[36] TMB was oxidized in presence of hydroxyl radicals (OH) formed when Cu ions react with H_2O_2 in acidic media. Briefly, PtCu NPs (0.05 mg mL^{-1}) was stirred to release Cu ions for 48 h in the presence of GSH (5 mM). Subsequently, the supernatant was collected, diluted in PBS buffer, and mixed with 10 μL of TMB (10 mg mL^{-1}in DMSO) in the presence of H_2O_2 (1 mM). TMB oxidation was monitored using UV–vis absorption of TMB in 652 nm.[22a]

Catalase Enzyme-Mimicking Activity to Generate Molecular O_2:   The catalase-mimicking behavior of PtCu nanostructures was evaluated to generate O_2 from hydrogen peroxide (1 mM). The catalytic properties were evaluated using a concentration of 0.05 mg mL^{-1} (1 mL) of PtCu NPs in a 2 mL vial. O_2 concentration levels were monitored with the aid of an oximeter.

Photothermal Heating Experiments: All the PT heating experiments were conducted using 96 well cell culture plates and 0.2 mL of an aqueous solution with a concentration of 0.05 mg mL^{-1}, of either PtCu NPs or Pt hollow nanoframes subjected to irradiation with an 808 nm laser using power = 0.44 W cm^{-2} unless otherwise specified. To monitor the temperature over time, a thermocouple was placed in the outer border of the plates to minimize the direct impact of the laser beam.

Cell Cultures and In Vitro Cytotoxicity Assays: Glioblastoma cells (U251-MG), cervical cancer cells (HeLa) and melanoma cells (B16-F10) were provided by cell services from Cancer Research-UK. They were cultured in Dulbecco's modified Eagle's medium (DMEM) with 10% of FBS (GIBCO), supplemented with 1% penicillin/streptomycin and 1% amphotericin (Biowest, France) and maintained at 37 °C in humidified atmosphere under normoxic conditions. To determine the tolerability and the cytotoxic properties of the PtCu NPs and the Pt nanoframes, the Blue Cell Viability Assay Kit (Abnova) was employed following the manufacturer's instructions. To carry out the test, the two cell lines were seeded at a density of 4×10^3 cells per well (into a 96-well plate) in 100 μL of the previously mentioned medium. After incubation at 37 °C for 24 h, the medium was changed to 100 μL of freshly prepared medium enriched with PEGylated PtCu NPs and Pt hollow nanoframes (1.6, 3.12, 6.25, 12.5, and 25 μg mL^{-1}, (Expressed in total Pt concentration (Elemental Analysis))) and the cells were cultured for another 3, 6, 24, and 48 h. At these different time-points, cells were washed twice with PBS and then treated with the Blue Cell viability Assay test (10% v/v in cell cultured media) for 90 min. Briefly, Blue Cell

**ADVANCED
SCIENCE NEWS**

www.advancedsciencenews.com

**ADVANCED
FUNCTIONAL
MATERIALS**

www.afm-journal.de

reagent, like other resazurin-based assays, utilizes the redox dye resazurin which is not fluorescent, but upon reduction by metabolically active and live cells is converted into a highly fluorescent product (resorufin). Non-treated cells were considered as 100% of cell viability. Fluorescence emission was detected using a PerkinElmer EnVision 2101 multilabel reader (Ex/Em: 540/590 nm). Experiments were performed in triplicates.

In Vitro Internalization Assays: Confocal Microscopy and MP-AES Analysis: The cellular uptake and the trafficking of PtCu NPs and Pt hollow nanoframes in U251-MG, HeLa and B16-F10 cells were evaluated by confocal microscopy (Spectral Confocal Microscope Zeiss LSM 880 with Airyscan) with a 63x oil immersed objective. Cells were seeded at a density of 2.5×10^4 onto 20 mm cover slips (in a 24-well plate) and incubated under standard culture conditions for 24 h. Then, 6.25 µg mL^{-1} of PtCu NPs and Pt NFs was added to each well and incubated for 3, 6, 4, 24, and 48 h. The cells were fixed with 4% paraformaldehyde during 30 min at RT, and stained with phalloidin-Alexa488 (Invitrogen) and Draq-5. The cells were imaged by confocal microscopy. The reflection of the incident light at Ex/Em of 488/490 nm was used to directly PtCu NPs and Pt NFs. Z-stack orthogonal projections were also carried out to enable visualization of the NPs inside cells cytosol.

In Vitro Cell Irradiation: Photothermal Effect of PtCu Nanostructures and Pt Nanoframes: To study the laser photothermal effect, U251-MG, HeLa, and B16-F10 cells were seeded (4×10^3) onto a 96-well plate for 24 h before the incubation with PtCu NPs and Pt NFs (12.5 µg mL^{-1}). The nanomaterials were incubated with the cells for 24 h. To reduce any possible heating potentially produced by non-internalized nanostructures present in the medium, cells were washed twice with PBS and replaced with fresh cell media. All the cell cultures were then irradiated during 20 min with a NIR laser (808 nm) at 2.5 W cm^{-2} of irradiance. The temperature increment in cell cultures was also measured during NIR irradiation with a thermocouple. Then, cells were incubated with the Blue Cell Viability Assay Kit (as mentioned above) to determine the death caused by the PTT effect. To study in more detail the potential therapeutic effect caused by the laser application after the incubation of the nanostructures, apoptosis and necrosis cell death mechanisms were investigated by flow cytometry (Gallios Flow Cytometer, Beckman Coulter). To this end, the irradiated cells were collected and the final pellet was suspended in PBS. The analysis of cell apoptosis and necrosis was developed through a double-staining with Annexin V-FITC (5 µL) and propidium iodide (5 µL) during 15 min prior to their analysis by flow cytometry. Control samples (non-treated cells, laser irradiated cells and cells treated with the nanostructures but in the absence of laser) were also tested as control samples.

Intracellular GSH and ROS Quantification: To quantify the intracellular GSH concentration, U251-MG, HeLa, and B16-F10 cells were seeded in culture dishes upon they reach 80% of confluence. Cells were then treated with PtCu NPs (6.25 and 25 µg mL^{-1}) during 24 h. After this time cells were collected and washed with PBS (500 g, 5 min). Supernatant was discarded and GSH levels were then measured in cell pellets. To this end, the pellet was resuspended in 1 mL of PBS and subjected to ultrasounds using a probe sonicator for 1 min to ensure cell membrane rupture. After sonication, the samples were filtered to remove any solids. The resulting filtrates were then transferred to UPLC vials for analysis. Quantification and identification of the GSH were performed using ultra-performance liquid chromatography coupled with mass spectrometry (UPLC-MS). Chromatographic separation was carried out at 40 °C using an ACQUITY UPLC BEH C18 column (130 Å, 1.7 µm, 2.1 × 50 mm, WATERS) under isocratic conditions with a mobile phase composed of 50% acetonitrile and 50% Milli-Q water, delivered at a flow rate of 0.3 mL min^{-1}.

For the in vitro analysis of the ROS production, U251-MG, HeLa, and B16-F10 cells (2.5×10^4) were seeded onto 20 mm cover slips (in a 24-well plate) and incubated under standard culture conditions. After 24 h, PtCu NPs (6.25 and 25 µg mL^{-1}) were added during 24 h. After that, cells were incubated with CellROX Green probe (ThermoFisher Scientific, USA). CellROX probe was added at a final concentration of 5 µM and incubated for 30 min at 37 °C, following manufacturer's instructions. Finally, cells were fixed with 4% paraformaldehyde during 30 min at RT, and they were assembled in a slide with FluoromontG and DAPI (ex/em 364/454) for confocal microscopy analysis (Spectral Confocal Microscope Zeiss LSM 880 with Airyscan with a 63x oil immersed objective). ROS semiquantification was conducted by evaluating the fluorescence pixel intensity in the green channel of confocal images.

In Vivo Experiments: All the procedures of this study were performed under the Project Licenses PI 12/24 approved by the Ethic Committee for Animal Experiments from the University of Zaragoza (Comisión Ética Asesora para la Experimentación Animal de la Universidad de Zaragoza). Mice were fed ad libitum and their care and maintenance under specific pathogen-free conditions were performed accordingly with the Spanish Policy for Animal Protection RD53/2013, which meets the European Union Directive 2010/63 on the protection of animals destined to experimental and other scientific purposes.

For these experiments 6- to 8-week-old female BALB/c nu/nu mice (Envigo) were employed. All the animals were maintained under quarantine during 7 days as soon as they arrived to the animal facilities and before starting the experiments. For the inoculation of the xenograft model, animals received a subcutaneous injection of 5×10^6 U251-MG cells suspended in 200 µL of DPBS. In order to evaluate potential weight loss during the experiments, mice were weighed daily. Tumors were measured with a caliper. Two different and independent experiments were carried out in order to evaluate the biodistribution and the toxicity of the PtCu NPs and to assess the efficiency of the PTT therapeutic approach. The manipulation of the animals during the procedures was performed under sterile conditions in a hood.

In the biodistribution experiments after 9 days of tumor implantation, 5 mg kg^{-1} of PtCu NPs were administered intratumorally. Then, mice were divided in 3 groups according to their day of death (7 animals per group): group 1, group 2, and group 3 were sacrificed after 24 , 48 h, and 1 week after the PtCu NPs injection, respectively. Animals were euthanized by CO$_2$ inhalation at the time points indicated before.

Tumor, kidneys, liver, lungs, spleen, and pancreas were collected from each animal for histopathological analysis (described later) and to evaluate metal bioaccumulation by ICP-MS. To quantify the amount of metal, each organ was digested with aqua regia (from 1 to 6 mL depending on the volume of the organ) for 5 days at room temperature. Then, the samples were diluted 1/5 in miliQ H$_2$O and total amount of the metals (Pt and Cu) present within the tissues were determined by ICP-MS and/or by ICP-OES (Perkin Elmer Elan DRC-e) in the Chemical Analysis Service from the University of Zaragoza.

In the in vivo photothermal studies, the animals were divided in four groups (8 animals per group): group 1: control without PtCu NPs and without laser irradiation; group 2: control without PtCu NPs and with laser irradiation; group 3: control with addition of PtCu NPs without laser irradiation; and group 4: addition of PtCu NPs and laser irradiation. During the irradiation, animals were initially anesthetized with 5% isoflurane and maintained with 1%–2% isoflurane (1 L min^{-1} oxygen flow). Irradiation was performed within a sterile hood while resting on an electric pad to avoid hypothermia when animals were exposed to anesthesia. 9 days after the tumor implantation, 5 mg kg^{-1} of PtCu NPs were intratumorally administered to mice from groups 3 and 4. Then, 48 h later, groups 2 and 4 were irradiated with a NIR-laser (808 nm) at a power of 1.5 W during 40 s. The temperature was monitored at different time points during the irradiation (0, 20, and 40 s) with a temperature sensor and in some cases with a thermographic camera. Tumor size was periodically evaluated by using a caliper. Aloe Vera VET was cutaneously applied to the tumors of animals treated with the laser in order to promote the healing of the wound caused by the laser (in the case of group 4).

One week after the first PtCu NPs administration, NPs were again intratumorally administered (5 mg kg^{-1}) in the mice tail and 48 h after their administration, they were irradiated with the laser (1 W during 40 s). Tumor size was assessed using a caliper and Aloe Vera VET was also cutaneously applied to the tumors. Tumor size was measured with a caliper during the next 21 days after tumor implantation. For the histopathological analysis, the euthanasia of the animals was performed by CO$_2$ inhalation. Then, tumor, kidneys, liver, lungs, spleen, and pancreas were collected.

In the biodistribution experiments, samples were fixed in 4% formaldehyde (Alfa Aesar) for 24 h, followed by cold 70% ethanol. Tissue

samples were then embedded in paraffin and three micrometer sections were stained with hematoxylin and eosin (HE). The presence of the PtCu NPs in the organs was visualized under an inverted microscope (Olympus IX81).

In order to confirm the presence of PtCu NPs in the tumors, an immunofluorescence analysis by confocal microscopy was carried out (Zeiss LSM 880). To this end, samples were frozen with isopentane cooled by liquid nitrogen and cryo-sectioned at 5 micrometres. Slices were assembled in a slide with FluoromontG and DAPI (ex/em 364/454) for visualization and visualized by confocal microscopy (Spectral Confocal Microscope Zeiss LSM 880 with Airyscan). NPs were directly visualized by reflexion of the incident light.

In the PT studies, 3 micrometer sections of the organs were stained with HE as previously mentioned. To assess tumour proliferation and remission, an immunohistochemical evaluation was performed by using a human Ki-67 antibody (Agilent). The automated immunostaining platform Autostainer Link (Dako) was employed. Sections (4–5 µm) were dewaxed and rehydrated with dH_2O and antigen retrieval was performed by heating at pH 7 for 20 min. Samples were incubated with primary Ki-67 antihuman antibody during 20 min, followed by the visualization system conjugated with horseradish peroxidase (Flex/HRP system, Agilent) using haematoxylin staining as contrast agent. Finally, sections were dehydrated and mounted. Samples were visualized under a conventional microscopy (Widefield inverted microscope Olympus IX81). Ki-67 protein expression was assessed in all mice groups by counting positive and negative cells in three acquisition images from all animals from each group using ImageJ software to obtain the percentage of positive cells.

For the evaluation of the apoptosis, caspase 3 labelling was carried out. After antigen retrieval in TRIS-EDTA at pH 9 solution for 20 min at 97 °C (PT Link; Dako), the immunohistochemistry with caspase 3 antibody was performed. With this aim, firstly the endogenous peroxidase was blocked during 10 min with two washing steps with Dako washing buffer. Afterward, samples were incubated with the primary antibody anti-caspase 3 (Rabbit policlonal, RyD Systems) diluted 1/125 during 30 min at room temperature, followed by the visualization system with the ImmPRESS HRP Horse Anti-Rabbit IgG Polymer Detection Kit and Peroxidase (VectorLabs, MP-7401). Finally, after three washing steps (Dako wash buffer, 5 min each) 3,3′-diaminobenzidine (DAB) was used for signal detection and hematoxylin for contrast.

Immunohistochemistry of CCR2 was performed following the same procedure as the one for anti-caspase 3. The employed antibody was anti-CCR2 anti-mouse (rabbit, Novus Biologicals) diluted 1/1500 during 40 min at room temperature.

For the necrosis study, CD40 labelling was employed. In this case, the antigen retrieval was carried out using citrate at pH 6 during 20 min at 97 °C (PT Link; Dako). Anti-CD40/ TNFRSF5 anti-mouse (Goat, RyD Sytems) was diluted 1/14 and incubated during 60 min at room temperature. Then, the secondary antibody Rabbit anti-Goat HRP (Dako agylent) was incubated (1/200) and the visualization was carried out as described before.

The activation of the immune system was assessed by staining CD45R. The antigen retrieval was carried out using citrate at pH 6 during 20 min at 97 °C (PT Link; Dako). Then, anti-CD45R anti-mouse (Rat, Invitrogen Thermo, 1/200) was incubated during 30 min at room temperature before the addition of the secondary antibody (Rabbit anti-Rat HRP (Dako Agilent, 1/500) during 30 min. For the visualization, EnVision+ Single Reagents HRP. Rabbit (Dako Agilent) was used.

The experimental approach summarizing the time points, the analysis and the sampling is included in Figure S14 (Supporting Information).

Statistical Analysis: The biological experiments were performed in triplicate. All the data are indicated as mean ± SD. Statistical analysis of the significant differences among the means were analyzed by one-way or two-way analysis of variance (ANOVA) for multiple comparisons by Dunnett's multiple comparisons test (GraphPad Prism Software). Statistically significant differences were expressed as follows: $^*p < 0.05$; $^{**}p < 0.01$; $^{***}p < 0.001$ y $^{****}p < 0.0001$.

Supporting Information

Supporting Information is available from the Wiley Online Library or from the author.

Conflict of Interest

The authors declare no conflict of interest.

Data Availability Statement

The data that support the findings of this study are available from the corresponding author upon reasonable request.

[1] A. Lujambio, S. W. Lowe, *Nature* **2012**, *482*, 347.
[2] a) A. Schroeder, D. A. Heller, M. M. Winslow, J. E. Dahlman, G. W. Pratt, R. Langer, T. Jacks, D. G. Anderson, *Nat. Rev. Cancer* **2012**, *12*, 39; b) T. Lammers, F. Kiessling, M. Ashford, W. Hennink, D. Crommelin, G. Storm, *Nat. Rev. Mater.* **2016**, *1*, 16069; c) C. Sawyers, *Nature* **2004**, *432*, 294.
[3] Y. Barenholz, *J. Controlled Release* **2012**, *160*, 117.
[4] G. Song, L. Cheng, Y. Chao, K. Yang, Z. Liu, *Adv. Mater.* **2017**, *29*, 1700996.
[5] Z. Hu, S. Wang, Z. Dai, H. Zhang, X. Zheng, *J. Mater. Chem. B* **2020**, *8*, 5351.
[6] a) H. Kim, K. Chung, S. Lee, D. H. Kim, H. Lee, *WIREs Nanomed. Nanobiotechnol.* **2016**, *8*, 23; b) D. K. Chatterjee, L. S. Fong, Y. Zhang, *Adv. Drug Delivery Rev.* **2008**, *60*, 1627.

[7] W. Zeng, H. Zhang, X. Yuan, T. Chen, Z. Pei, X. Ji, *Adv. Drug Delivery Rev.* **2022**, *184*, 114241.

[8] X. Qian, Y. Zheng, Y. Chen, *Adv. Mater.* **2016**, *28*, 8097.

[9] D. J. Irvine, E. L. Dane, *Nat. Rev. Immunol.* **2020**, *20*, 321.

[10] a) E. R. Sauter, *Expert Rev. Clin. Pharmacol.* **2020**, *13*, 265; b) I. Melero, D. M. Berman, M. A. Aznar, A. J. Korman, J. L. P. Gracia, J. Haanen, *Nat. Rev. Cancer* **2015**, *15*, 457.

[11] a) H. Zhang, W. Li, X. Guo, F. Kong, Z. Wang, C. Zhu, L. Luo, Q. Li, J. Yang, Y. Du, J. You, *ACS Appl. Mater. Interfaces.* **2017**, *9*, 20385; b) X. Wang, X. Zhong, Z. Liu, L. Cheng, *Nano Today* **2020**, *35*, 100946; c) J. M. Hortin, A. J. Anderson, D. W. Britt, A. R. Jacobson, J. E. McLean, *Environ. Sci.: Nano* **2020**, *7*, 2618.

[12] a) D. Cassano, A.-K. Mapanao, M. Summa, Y. Vlamidis, G. Giannone, M. Santi, E. Guzzolino, L. Pitto, L. Poliseno, R. Bertorelli, V. Voliani, *ACS Appl. Bio Mater.* **2019**, *2*, 4464; b) B. Rubio-Ruiz, A. M. Pérez-López, L. Uson, M. C. Ortega-Liebana, T. Valero, M. Arruebo, J. L. Hueso, V. Sebastian, J. Santamaria, A. Unciti-Broceta, *Nano Lett.* **2023**, *23*, 804.

[13] a) S. Ali, A. S. Sharma, W. Ahmad, M. Zareef, M. M. Hassan, A. Viswadevarayalu, T. Jiao, H. Li, Q. Chen, *Crit. Rev. Anal. Chem.* **2021**, *51*, 454; b) Y. Tan, D. Huang, C. Luo, J. Tang, R. T. K. Kwok, J. W. Y. Lam, J. Sun, J. Liu, B. Z. Tang, *Nano Lett.* **2023**, *23*, 7683.

[14] a) J. I. Garcia-Peiro, P. Guerrero-López, F. Hornos, J. L. Hueso, J. M. Garcia-Aznar, J. Santamaria, *Small Sci.* **2024**, *4*, 2400206; b) H. Moon, D. Kumar, H. Kim, C. Sim, J.-H. Chang, J.-M. Kim, H. Kim, D.-K. Lim, *ACS Nano* **2015**, *9*, 2711; c) Q. Wang, H. Wang, Y. Yang, L. Jin, Y. Liu, Y. Wang, X. Yan, J. Xu, R. Gao, P. Lei, J. Zhu, Y. Wang, S. Song, H. Zhang, *Adv. Mater.* **2019**, *31*, 1904836.

[15] a) S. Zhang, L. Nguyen, J.-X. Liang, J. Shan, J. Liu, A. I. Frenkel, A. Patlolla, W. Huang, J. Li, F. Tao, *Nat. Commun.* **2015**, *6*, 7938; b) C. H. Wu, C. Liu, D. Su, H. L. Xin, H.-T. Fang, B. Eren, S. Zhang, C. B. Murray, M. B. Salmeron, *Nat. Catal.* **2019**, *2*, 78.

[16] J.-H. Zhong, X. Jin, L. Meng, X. Wang, H.-S. Su, Z.-L. Yang, C. T. Williams, B. Ren, *Nat. Nanotechnol.* **2017**, *12*, 132.

[17] J. Bonet-Aleta, M. Encinas-Gimenez, E. Urriolabeitia, P. Martin-Duque, J. L. Hueso, J. Santamaria, *Chem. Sci.* **2022**, *13*, 8307.

[18] J. Bonet-Aleta, J. V. Alegre-Requena, J. Martin-Martin, M. Encinas-Gimenez, A. Martín-Pardillos, P. Martin-Duque, J. L. Hueso, J. Santamaria, *Nano Lett.* **2024**, *24*, 4091.

[19] H. Y. Kim, T. Kwon, Y. Ha, M. Jun, H. Baik, H. Y. Jeong, H. Kim, K. Lee, S. H. Joo, *Nano Lett.* **2020**, *20*, 7413.

[20] a) J. I. Garcia-Peiro, J. Bonet-Aleta, J. Santamaria, J. L. Hueso, *Chem. Soc. Rev.* **2022**, *51*, 7662; b) J. I. Garcia-Peiro, J. Bonet-Aleta, M. L. Tamayo-Fraile, J. L. Hueso, J. Santamaria, *Nanoscale* **2023**, *15*, 14399; c) J. I. Garcia-Peiro, M. C. Ortega-Liebana, C. Adam, Á. Lorente-Macías, J. Travnickova, E. E. Patton, P. Guerrero-López, J. M. Garcia-Aznar, J. L. Hueso, J. Santamaria, A. Unciti-Broceta, *Angew. Chem., Int. Ed.* **2025**, *n/a*, 202424037.

[21] a) Z. Zhou, K. Hu, R. Ma, Y. Yan, B. Ni, Y. Zhang, L. Wen, Q. Zhang, Y. Cheng, *Adv. Funct. Mater.* **2016**, *26*, 5971; b) J. Li, X. Zu, G. Liang, K. Zhang, Y. Liu, K. Li, Z. Luo, K. Cai, *Theranostics* **2018**, *8*, 1042.

[22] a) X. Zhong, X. Wang, L. Cheng, Y. Tang, G. Zhan, F. Gong, R. Zhang, J. Hu, Z. Liu, X. Yang, *Adv. Funct. Mater.* **2020**, *30*, 1907954; b) S. Cheng, L. Chen, F. Gong, X. Yang, Z. Han, Y. Wang, J. Ge, X. Gao, Y. Li, X. Zhong, L. Wang, H. Lei, X. Zhou, Z. Zhang, L. Cheng, *Adv. Funct. Mater.* **2023**, *33*, 2212489.

[23] R. Castillo, E. D. Garcia, J. L. Santos, M. A. Centeno, F. Romero Sarria, M. Daturi, J. A. Odriozola, *Catal. Today* **2020**, *356*, 390.

[24] K. Ji, L. Mayernik, K. Moin, B. F. Sloane, *Cancer Metastasis Rev.* **2019**, *38*, 103.

[25] D. Fang, L. Wan, Q. Jiang, H. Zhang, X. Tang, X. Qin, Z. Shao, Z. Wei, *Nano Res.* **2019**, *12*, 2766.

[26] Z. Zhang, Z. Luo, B. Chen, C. Wei, J. Zhao, J. Chen, X. Zhang, Z. Lai, Z. Fan, C. Tan, M. Zhao, Q. Lu, B. Li, Y. Zong, C. Yan, G. Wang, Z. J. Xu, H. Zhang, *Adv. Mater.* **2016**, *28*, 8712.

[27] F. Nosheen, Z.-c. Zhang, J. Zhuang, X. Wang, *Nanoscale* **2013**, *5*, 3660.

[28] H.-J. Niu, H.-Y. Chen, G.-L. Wen, J.-J. Feng, Q.-L. Zhang, A.-J. Wang, *J. Colloid Interface Sci.* **2019**, *539*, 525.

[29] J. Bonet-Aleta, M. Sancho-Albero, J. Calzada-Funes, S. Irusta, P. Martin-Duque, J. L. Hueso, J. Santamaria, *J. Colloid Interface Sci.* **2022**, *617*, 704.

[30] S. Mehmood, U. E. Klotz, G. Pottlacher, *Metall. Mater. Trans. A* **2012**, *43*, 5029.

[31] B. Ma, S. Wang, F. Liu, S. Zhang, J. Duan, Z. Li, Y. Kong, Y. Sang, H. Liu, W. Bu, L. Li, *J. Am. Chem. Soc.* **2019**, *141*, 849.

[32] B. Guo, F. Yang, L. Zhang, Q. Zhao, W. Wang, L. Yin, D. Chen, M. Wang, S. Han, H. Xiao, N. Xing, *Adv. Mater.* **2023**, *35*, 2212267.

[33] E. J. Ge, A. I. Bush, A. Casini, P. A. Cobine, J. R. Cross, G. M. DeNicola, Q. P. Dou, K. J. Franz, V. M. Gohil, S. Gupta, S. G. Kaler, S. Lutsenko, V. Mittal, M. J. Petris, R. Polishchuk, M. Ralle, M. L. Schilsky, N. K. Tonks, L. T. Vahdat, L. Van Aelst, D. Xi, P. Yuan, D. C. Brady, C. J. Chang, *Nat. Rev. Cancer* **2022**, *22*, 102.

[34] H. M. Ragab, N. Samy, M. Afify, N. A. El Maksoud, H. M. Shaaban, *J. Gen. Eng. Biotechnol.* **2018**, *16*, 479.

[35] Y. Zhang, X. Zhan, J. Xiong, S. Peng, W. Huang, R. Joshi, Y. Cai, Y. Liu, R. Li, K. Yuan, N. Zhou, W. Min, *Sci. Rep.* **2018**, *8*, 8720.

[36] B. Niu, K. Liao, Y. Zhou, T. Wen, G. Quan, X. Pan, C. Wu, *Biomaterials* **2021**, *277*, 121110.